Study of brittle fracture by acoustic emission from indentation cracks

Cite as: Journal of Applied Physics **65**, 4234 (1989); https://doi.org/10.1063/1.343306
Submitted: 15 August 1988 • Accepted: 01 February 1989 • Published Online: 17 August 1998

Kwang Yul Kim and Wolfgang Sachse

Study of brittle fracture by acoustic emission from indentation cracks

Kwang Yul Kim and Wolfgang Sachse
Department of Theoretical and Applied Mechanics, Cornell University, Ithaca, New York 14853

(Received 15 August 1988; accepted for publication 1 February 1989)

This paper describes a novel approach for investigating the fracture of brittle solids by combining a theory of acoustic emission (AE) with the Dugdale–Barenblatt model. An example is provided with indentation-produced, half-penny-shaped cracks that were generated by pressing a Vickers indenter onto the surface of a glass plate and that produced AE signals. These were detected using four capacitive displacement transducers, one at epicenter and the other three at off-epicentral positions. Assuming that a mode I type of crack was generated and using indentation fracture mechanics, a mode I stress intensity factor $K_{Ic} = 7.44 \times 10^5$ N/m$^{3/2}$ was obtained. Both dipole strength and source-time function associated with crack formation were determined from the AE theory. Assuming that an effective gauge length can be interpreted equal to a dipole linkage distance and using the Dugdale–Barenblatt model for the fracture of brittle solids, it is shown that all the other important parameters on crack formation can be determined. Included are the critical rupture stress $\sigma_c = 8.94$ GPa, the crack tip opening displacement of 1.62 nm, the effective microstructural gauge length equal to 13.2 nm, and the time-dependent crack velocity as a function of a crack front radius.

I. INTRODUCTION

Vickers indenters are widely used in the hardness testing of materials. Two important parameters needed for determination of the Vickers hardness of the test specimen are the diagonal of the impression and the applied load. This test procedure has recently been extended to the study of fracture of brittle solids[1–4] using the Vickers indenter to generate microcracks on the surface as it is pressed onto the surface. Because the test is easy and simple to perform and many tests can be made in small specimens that are unsuitable for conventional fracture toughness testing, the indentation test has increasingly been applied for the fracture toughness testing of brittle materials such as glass, ceramic, and semiconducting materials.

Several years ago, we investigated the acoustic emission (AE) signals emanating from a penny-shaped crack that was generated with a sharp indenter of conical shape.[5,6] From analysis of the emitted signals we determined the radiation pattern, moment tensor components, and the source-time function associated with crack formation. We demonstrated that the radiation pattern of AE signals can be used to determine the orientation of the crack formed, while the source-time function provides information on the velocity of microcracks whose formation occurs on a submicrosecond time scale.

In this paper we study the AE signals detected when the Vickers indenter is pressed against the surface of a soda-lime glass plate, which results in two mutually perpendicular cracks of half-penny shape as depicted in Figs. 1(a) and 1(b). The experimental procedure for generating and detecting the AE signals emitted during the formation of these cracks is described in Sec. II. The determination of the source-time function and the dipole strength were carried out by assuming that the cracks generated by the Vickers indenter were of mode I type. From the measured applied load and crack size, the mode I stress intensity factor K_{Ic}, and hence the fracture toughness of soda-lime glass, were also obtained. In Sec. III we establish a relationship between the fracture toughness and the dipole strength associated with crack formation, from which all of the relevant data on the formation of the crack, including the critical rupture stress and strain, the length of the microstructural linkage unit, or dipole linkage distance and the critical crack tip opening displacement (CTOD) can be determined. These data are presented in Sec. IV. Section V discusses the time-

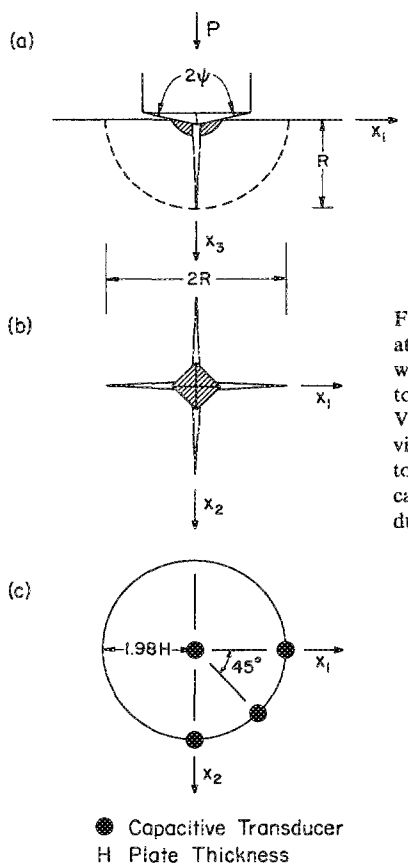

FIG. 1. System of crack generation and transducer location, where x_1 and x_2 axes are chosen to be along the diagonals of the Vickers indenter. (a) A side view of the crack system. (b) A top view of the crack. (c) Location of the capacitive transducers.

 0021-8979/89/114234-11$02.40

dependent crack velocity and its dependence on the radius of the crack front.

II. EXPERIMENTAL PROCEDURE

The specimen in which the Vickers indentation cracks (VIC) were generated was a soda-lime glass plate that was 0.960 cm thick ($\equiv H$) and approximately 16 cm square. The specimen was mounted in a specially constructed loading jig that permitted the simultaneous measurement of the load applied to the top surface of the glass plate through the Vickers indenter via a miniature load cell with the detection of the crack signals by the capacitive transducers. The load cell had a maximum capacity of 225 N with a resolution of 6×10^{-3} N. The bottom side of the glass plate was coated with 0.3-μm-thick chromium film which served as a ground plane for the capacitive displacement transducers attached to it. The loading through the Vickers indenter was basically a soft, force-controlled loading. As the load through the indenter was gently and gradually increased to a certain critical level, two mutually perpendicular cracks, both normal to the surface, suddenly initiated beneath the sharp indenter tip and propagated outward in planes aligned with the diagonals of the indenter. The shape of the resulting cracks was a half-penny as depicted in Fig. 1(a). Formation of these cracks gave rise to elastic waves that propagated through the plate to the bottom surface where they were detected by four capacitive transducers.[7] Location of these transducers are shown in Fig. 1(c). One was located at epicenter and the other three were situated at a distance of $1.98H$ units away from the epicenter at an equal distance on the opposite side from the AE source at angular positions $\theta = 0°$, 45°, and 90°, where the angle θ was measured from the x_1 axis whose direction was chosen normal to the plane of one of the generated cracks. Immediately after detecting the first AE signals associated with crack formation, the indenter was gently and slowly removed from the specimen, which was then moved to other locations for generation of subsequent cracks.

The entire electronic diagram of the AE detection system is shown schematically in Fig. 2. The signals detected by the capacitive transducers were amplified by charge amplifiers whose bandwidth extended from 10 kHz to 10 MHz and whose voltage/charge sensitivity was 0.250 V/pC. The outputs of the charge amplifiers were connected to transient recorders for digitization at a sampling rate of 60 MHz and with 10-bit resolution. The transient recorder connected to the epicentral transducer also served as the external trigger source for the recorders of the off-epicentral signals. The recorded crack signals were transferred to a minicomputer-based data acquisition and processing system for subsequent signal processing and data reduction. Also connected to the data acquisition system was a 12-bit A/D converter which was used to digitize the load signal generated by the load cell at the time of crack formation. The data processing system also provided for storage of both the detected signals and processed data.

Prior to the formation of a crack, a glass capillary that had 0.05 mm i.d. and 0.08 mm o.d. was broken at the intended site of crack generation on the glass plate by pressing against it vertically with a razor blade through the same load

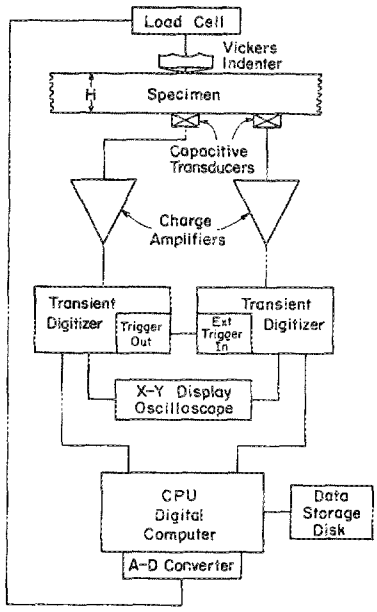

FIG. 2. Block diagram of the AE electronic system.

cell used with the Vickers indenter. The strength of the glass capillary fracture (GCF) was also measured by the load cell. Immediately following this, the indentation crack was induced to minimize the chance of disturbing the measurement system. The purpose of the capillary fracture, which generates axisymmetric AE signals, is twofold: First, it is used to compensate for the effects of variable sensitivity of the different transducers; second, it is used to determine the breaking strength of capillary fracture that is subsequently used for the determination of the dipole strength of the indentation cracks. These calculations will be explained in detail in the following sections.

Immediately after the test, the specimen was mounted on a microscope stage driven by fine micrometers with a translational resolution of 1 μm to determine the size of the indentation cracks. The results are listed in Table I. For each

TABLE I. Data of Vickers indentation cracks (VIC).

Crack No.	Applied load P (N)	Crack radii R_1 (mm)	Crack radii R_2 (mm)	Average radius R (mm)
VIC01	46.97	0.264	0.266	0.265
VIC02	48.35	0.267	0.275	0.271
VIC03	47.37	0.292	0.292	0.292
VIC04	37.75	0.241	0.239	0.240
VIC05	43.54	0.269	0.271	0.270
VIC06	35.79	0.239	0.246	0.243
VIC07	65.21	0.351	0.359	0.355
VIC08	58.55	0.327	0.339	0.333
VIC09	31.67	0.205	0.214	0.210
VIC10	52.76	0.283	0.298	0.291
VIC11	40.80	0.244	0.249	0.247
VIC12	68.84	0.352	0.368	0.360
VIC13	101.3	0.442	0.440	0.441
VIC14	55.11	0.290	0.301	0.295
VIC15	56.29	0.315	0.317	0.316
VIC16	32.07	0.219	0.217	0.218
VIC17	62.36	0.311	0.307	0.309
VIC18	53.25	0.324	0.325	0.325

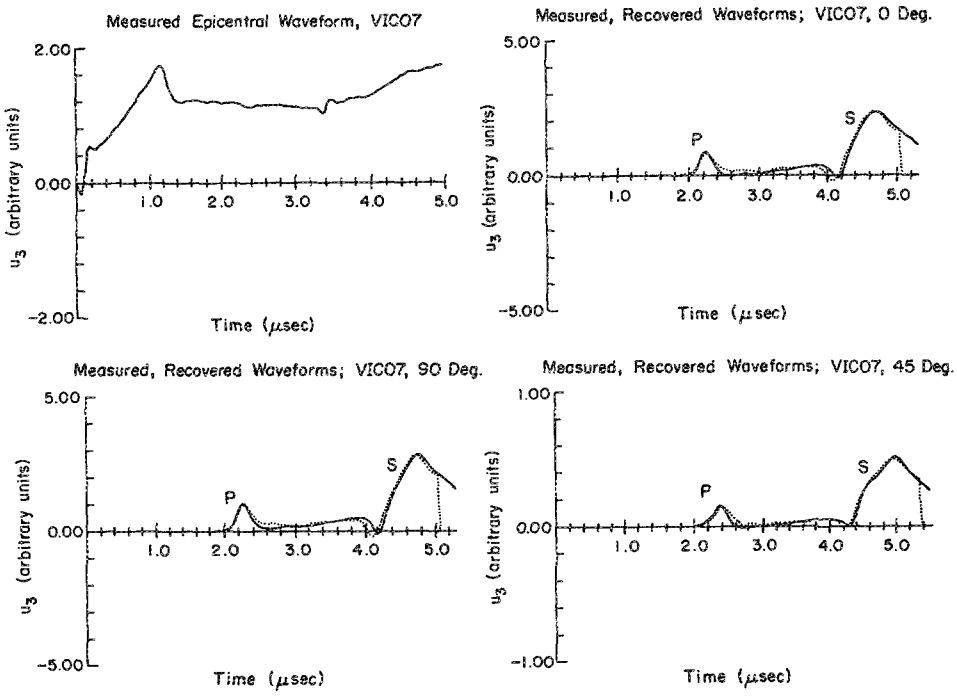

FIG. 3. Detected and regenerated crack AE waveforms at various locations. Solid lines are observed waveforms and dotted lines are theoretical. P denotes the arrival of the longitudinal wave and S represents that of the shear wave.

indentation the following information is listed: the applied load P, measured at the time of crack formation; the radii of the two mutually perpendicular cracks of half-penny shape R_1 and R_2; and the average of the two radii R equal to $(R_1 + R_2)/2$. A typical example of the AE crack signals emitted during the formation of the cracks is shown in Fig. 3 as solid curves. The signals generated during the glass capillary fracture (GCF) are displayed in Fig. 4 as solid lines. In these figures the ordinates correspond to the output of the charge amplifier which is proportional to the normal displacements on the surface of a specimen, u_3.

III. THEORY

A. Indentation fracture mechanics

The stress field produced beneath a sharp indenter was described in terms of the axisymmetric Boussinesq field by Lawn and co-workers.[1,2] At some critical load the crack initiates beneath the indenter tip and spontaneously breaks through to the free surface ("pop-in") and results in a well-developed, center-loaded, half-penny crack in the median plane, as shown in Fig. 1(a). Since an axisymmetric loading produces no shear stress in a median plane, only a tensile

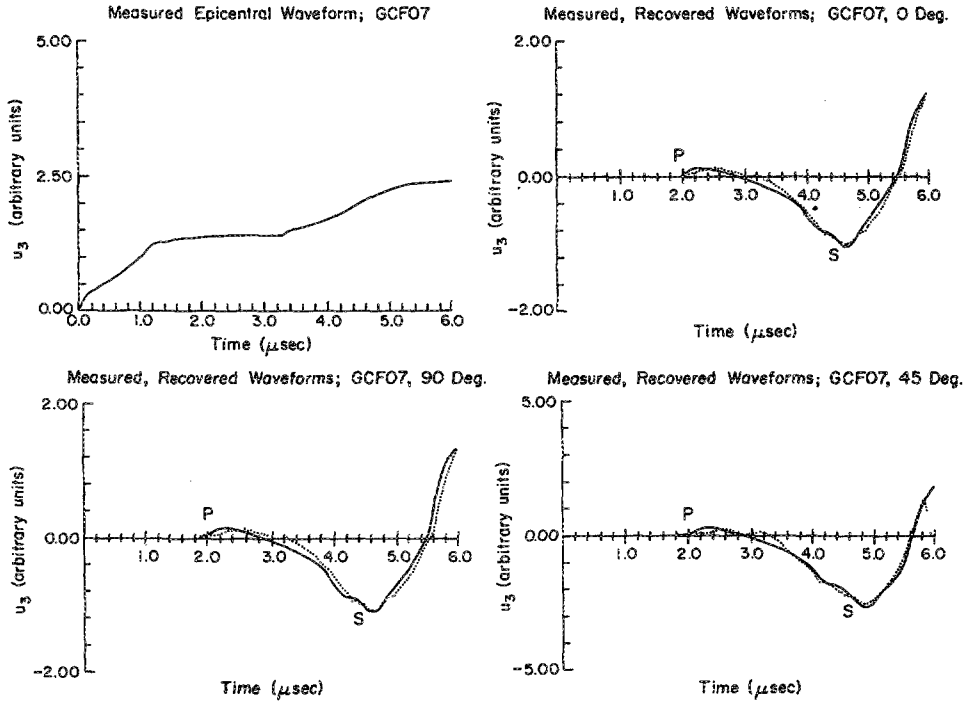

FIG. 4. Detected and recovered AE signals due to a glass capillary fracture at various locations. Observed waveforms are indicated with solid lines and recovered ones with dotted lines. P and S denote the arrivals of the longitudinal and shear waves, respectively.

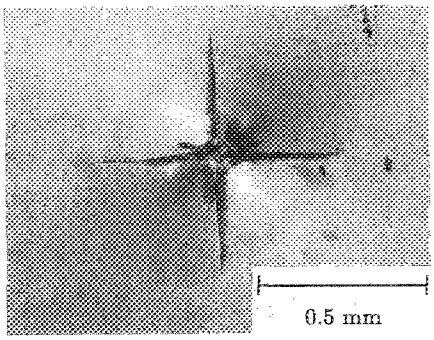

FIG. 5. An optical micrograph of the Vickers indentation crack no. 7 (top view) whose size is indicated in Table I. The small pyramidal shape shown in the center is the contact region of the indenter.

hoop stress acting on the median plane is responsible for the development of this crack, which is of mode I type. In our previous work,[5] we used the more realistic Sneddon solution in describing the hoop stress generated by the indentation of a conical indenter. Although the pyramidal Vickers indenter produces a slightly nonaxisymmetric field immediately beneath the contact region, the size of the pop-in crack is experimentally found to be much larger than the contact region (see Fig. 5) and the axisymmetric stress field is well suited for description of the stress field developed beneath the Vickers indenter. Since most of the crack formed is exposed to a free surface, one can safely neglect the contribution of the small shear stress beneath the contact region when the median crack forms.

Using dimensional analysis, Lawn and Fuller[1] derived a very simple expression for a stress intensity factor K_{Ic}:

$$K_{Ic} = \frac{1}{\pi^{3/2}\tan\psi}\left(\frac{P}{R^{3/2}}\right) = 7.256\times10^{-2}\left(\frac{P}{R^{3/2}}\right), \tag{1}$$

where P is the applied load, ψ is the half angle (68°) between the faces of the indenter, and R is the radius of the half-penny crack formed. The strain-energy release rate or the crack extension force G_c is then obtained, according to

$$G_c = K_{Ic}^2(1-\nu^2)/E, \tag{2}$$

where ν and E are the Poisson's ratio and Young's modulus of glass, which are, respectively, equal to 0.217 and 73.03 GPa. Equation (1) is strictly valid only for a conical indenter, but it has also been shown to yield a good fit to crack data obtained with a Vickers indenter.[1] When there is friction acting between the indenter and the specimen, ψ in Eq. (1) may be replaced by $\psi + \arctan\eta$, where η is the coefficient of friction. In the slow, gentle crack generation described here, which closely approximates a static loading, the effect of friction is assumed to be negligible. Equation (1) predicts that for a given material a plot of P vs $R^{3/2}$ will be a straight line and its slope yields a stress intensity factor.

We adopt the Dugdale–Barenblatt model[8–10] for calculation of G_c in Eq. (2). Referring to Fig. 6, it predicts for brittle solids that

$$G_c = \int_0^{u_c}\sigma(u)du = \int_0^{u_c}\sigma_c\frac{u}{u_c}du$$
$$= \tfrac{1}{2}\sigma_c u_c = \tfrac{1}{2}\sigma_c l\epsilon_c = 2\gamma. \tag{3}$$

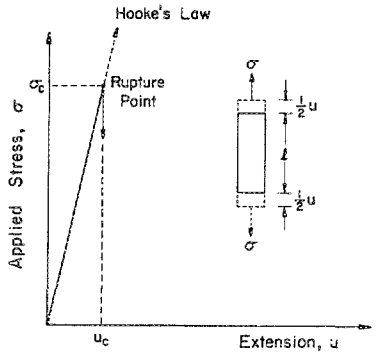

FIG. 6. An idealized stress-extension curve that indicates the cutoff stress and critical rupture extension for a perfectly brittle solid.

Here we have used the relation $\sigma(u) = \sigma_c u/u_c$ $(0\leqslant u\leqslant u_c)$, which is valid for a perfectly brittle solid. In the above equation, σ_c is a critical rupture stress which is approximately equal to $E/10$ for a perfectly brittle solid,[11] u_c is a critical crack tip opening displacement (CTOD), γ is the surface energy of the crack plane, and $l \equiv u/\epsilon = u_c/\epsilon_c$ is the length of a microstructural linkage unit[10] involved in the rupture process as illustrated in Fig. 6. For fracture of very brittle solids, to which the Barenblatt model is well adapted, l is the size of the cohesive zone surrounding the crack plane immediately ahead of the crack tip. The term ϵ_c is the cutoff strain at the time of rupture. The cutoff strain at the crack tip is given by

$$\epsilon_c = \sigma_c/E = u_c/l. \tag{4}$$

B. Dipole representation of an AE source from a mode I crack

The dopole representation of an AE source from a mode I indentation crack has been described in our previous publications[6] in terms of the diagonal components of the moment tensor discussed in the literature.[12,13] The moment tensor M_{ij} is conveniently expressed as[12,13]

$$M_{ij} = \int \Delta\sigma_{ij}\,dV, \tag{5}$$

where $\Delta\sigma_{ij}$ is the glut stress resulting in the source volume V. Equation (5) is quite general, that is, it holds regardless of whether the source region is subjected to elastic or nonlinear deformations.

We have also used this representation for an AE source accompanying the formation of a mode I thermal crack generated on the surface of a glass plate.[14] The essential requirement for using a diagonal representation of the moment tensor associated with a mode I crack is that one axis of the coordinate system used to represent the moment tensor is aligned with the crack normal and the other two axes are parallel to the plane of the crack. Otherwise, the moment tensor representing the AE source of a mode I crack must include off-diagonal elements as well. In the results to be described, the origin of the coordinate system is chosen to be the point of contact of the sharp Vickers indenter tip with the top surface of the glass plate when it touches the glass plate and the x_3 axis coincides with the loading direction. As shown in Fig. 1(b), two mutually perpendicular cracks are generated by the Vickers indentation for which the x_1 axis is chosen to be aligned normal to the first crack and the x_2 axis

normal to the other crack. With this coordinate system, the off-diagonal elements of the moment tensor associated with the mode I indentation crack vanish because no shear stresses contribute to the formation of a mode I crack. Then the moment tensor $\mathbf{M}$ associated with the Vickers indentation crack can be written in matrix form as

$$\mathbf{M} = (M_{ij}) = \begin{pmatrix} M_{11}(t) & 0 & 0 \\ 0 & M_{22}(t) & 0 \\ 0 & 0 & M_{33}(t) \end{pmatrix}, \tag{6}$$

where t represents time. The stress component σ_{33} acting under the contact region of the indenter gives rise to M_{33}, which, according to our past work,[6] is found to be only a few percent of M_{11} or M_{22}. Since most of the generated crack is exposed to a free surface at which σ_{33} is essentially zero, and the contact area is much smaller than the generated crack size (see Fig. 5), M_{33} can be set equal to zero with negligible error. The two cracks generated by a Vickers indentation are almost equal in size (see Table I) and therefore, both M_{11} and M_{22} should have almost equal magnitude, which we denote by D, or the dipole strength of the crack. Furthermore, the detected signals from these cracks indicate that their occurrence is almost simultaneous and hence we will assume that their formation takes place with the same temporal behavior described by the same source-time function. The source-time function associated with crack formation is generally known to be like a ramp step (cf. Fig. 9), similar to the characteristics of a Heaviside step, a linear ramp, or a parabolic ramp function with a certain rise time, but it is at this stage an unknown time function controlled by the energies of crack formation. We will normalize the steplike source-time function with risetime Δ_d and denote it by $\hat{S}^d(t)$, which has unit amplitude when $t \gg \Delta_d$. Expressing

$$M_{11}(t) = M_{22}(t) = D\hat{S}^d(t), \tag{7}$$

Eq. (6) can then be rewritten as

$$\mathbf{M} = D\begin{pmatrix} 1 & 0 & 0 \\ 0 & 1 & 0 \\ 0 & 0 & 0 \end{pmatrix}\hat{S}^d(t). \tag{8}$$

Then, a normal displacement $u_3^d(\mathbf{x},t)$ in the x_3 direction at a receiver location at $\mathbf{x}$ due to an AE dipole source acting at $\mathbf{x}_0$ can be conveniently expressed by means of the Green's function[12,15]:

$$u_3^d(\mathbf{x},t) = M_{ij} * G_{i3,j},$$

where a summation over repeated indices is implied. The factor $G_{ij,k}$, where $G_{ij,k} \equiv \partial G_{ij}/\partial x_k$ $(i,j,k = 1,2, \text{or } 3)$, represents the Green's function tensor and is called the dipole Green's function. The symbol "$*$" denotes a convolution integral in time. Thus,

$$u_3^d(\mathbf{x},t) = D\hat{S}^d(t) * [G_{13,1}(\mathbf{x},\mathbf{x}_0;t) + G_{23,2}(\mathbf{x},\mathbf{x}_0;t)] \tag{9}$$

$$= D\hat{S}^d(t) * G^d(\mathbf{x},\mathbf{x}_0;t), \tag{10}$$

where

$$G^d(\mathbf{x},\mathbf{x}_0;t) \equiv G_{13,1}(\mathbf{x},\mathbf{x}_0;t) + G_{23,2}(\mathbf{x},\mathbf{x}_0;t). \tag{11}$$

Let the polar-cylindrical angle θ be measured from the x_1 axis in the x_1x_2 plane. Then, the following radiation patterns hold in Eq. (9) according to Refs. 5 and 14:

$$\hat{S}^d(t) * G_{13,1}(\mathbf{x},\mathbf{x}_0;t) = a(t)[b(t) + \cos^2\theta], \tag{12}$$

$$\hat{S}^d(t) * G_{23,2}(\mathbf{x},\mathbf{x}_0;t) = a(t)[b(t) + \sin^2\theta], \tag{13}$$

where $a(t)$ and $b(t)$ are both independent of θ. Therefore,

$$u_3^d(\mathbf{x},t) = D\hat{S}^d(t) * G^d(\mathbf{x},\mathbf{x}_0;t) = Da(t)[2b(t) + 1]. \tag{14}$$

Equation (14) indicates that the radiation pattern obtained from receivers that are all located at different angles but at an equal distance from the source is expected to be a circle at a particular instant of time. Since the Vickers indenter penetrated slightly beneath the surface of the glass plate during the formation of the crack, the location of an AE source was conveniently given the coordinates $(0,0,0.01H)$ for the calculation of the Green's functions, which remain essentially unchanged for slight variations of the source depth. The Green's functions corresponding to the epicentral and off-epicentral receivers from the source are plotted in Figs. 7(a) and 7(b), respectively, using the P- (longitudinal) wave speed of 0.582 cm/μs and the S-(shear) wave speed of 0.350 cm/μs.

A displacement u_3^m at $\mathbf{x}$ due to a vertical force corresponding to a monopolar source acting at $\mathbf{x}_0$ with magnitude F_3, as in the case of a capillary fracture on the surface of a specimen, is in a similar fashion expressed as

$$u_3^m(\mathbf{x},t) = F_3\hat{S}^m(t) * G_{33}(\mathbf{x},\mathbf{x}_0;t), \tag{15}$$

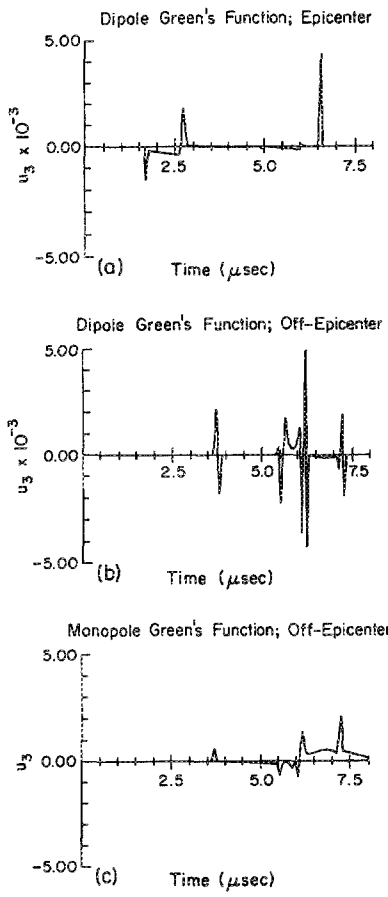

FIG. 7. Plate Green's functions: (a) The epicenter response due to a horizontal dipole source located at $(0,0,0.01H)$. (b) The response at $1.98H$ away from the epicenter due to a combination of two mutually perpendicular horizontal dipoles, both having equal magnitude and acting at $(0,0,0.01H)$. (c) The response at $1.98H$ away from epicenter due to a single vertical force acting at the origin.

where $\hat{S}^m(t)$ is the source-time function of the monopolar source with unit magnitude for $t \gg \Delta_m$ (rise time) and G_{33} is the appropriate monopole Green's function. The off-epicentral Green's function G_{33} corresponding to a monopolar source of single vertical force is also shown in Fig. 7(c).

The source-time functions $\hat{S}^d(t)$ and $\hat{S}^m(t)$, appearing in Eqs. (10) and (15), can be obtained by simply deconvoluting the measured displacement signal with the corresponding Green's function and normalizing the resulting time functions so that they have unit amplitude when $t \gg \Delta$. The dipole strength D can then be determined by performing a simple calibration experiment as described in Sec. III C.

C. Dipole strength

In this subsection we essentially follow a method described in Ref. 14 for determination of the strength of dipoles. The method is based on comparing the normal displacement response at a particular receiver corresponding to the formation of a crack with the response at the same receiver when a glass capillary fractures at a particular load. The receiver sensitivity is identical in both measurements. Let $\hat{u}_3^m$ and $\hat{u}_3^d$ represent, respectively, the nondimensional, normalized displacement at the particular receiver point of a specimen having unit thickness for the steplike source-time functions of unit magnitude $\hat{S}^m(t)$ and $\hat{S}^d(t)$. Similarly, let V_0^m and V_0^d be the corresponding voltage signals from the charge amplifier connected to the same capacitive displacement transducer measuring u_3^m and u_3^d in turn. Referring to Figs. 8 and 9, and using the work of Ceranoglu and Pao,[16] one obtains

$$V_0^m(t) = ku_3^m(t) = (kF_3/\pi\mu H)\hat{u}_3^m(t) = kF_3\hat{S}^m(t)*G_{33}(t), \tag{16}$$

$$V_0^d(t) = ku_3^d(t) = (kD/\pi\mu H^2)\hat{u}_3^d(t) = kD\hat{S}^d(t)*G^d(t), \tag{17}$$

where k is a constant independent of time and μ is the shear modulus of the specimen. With both $V_0^m(t)$ and $V_0^d(t)$ measured, and $G_{33}(t)$ and $G^d(t)$ theoretically calculated, $kF_3\hat{S}^m(t)$ and $kD\hat{S}^d(t)$ can now be calculated by the method of deconvolution:

$$kF_3\hat{S}^m(t) = V_0^m*(G_{33})^{-1}, \tag{18}$$

$$kD\hat{S}^d(t) = V_0^d*(G^d)^{-1}. \tag{19}$$

Noticing that both $\hat{S}^m(t)$ and $\hat{S}^d(t)$ approach unity when $t \gg \Delta$, one obtains

$$D = F_3\frac{[V_0^d*(G^d)^{-1}]|_{t\gg\Delta_d}}{[V_0^m*(G_{33})^{-1}]|_{t\gg\Delta_m}}. \tag{20}$$

The above equation, simple as it appears, was not used to determine D. The signal processing algorithms for finding the inverses of the Green's functions, i.e., $(G^d)^{-1}$ and $(G_{33})^{-1}$, appearing in the above equations have been developed.[17,18] Their application, however, to process experimental waveforms is not straightforward and hence an alternative procedure for determining the dipole strength appearing in Eq. (20) was developed.

Our signal processing programs implementing the deconvolution algorithms of Refs. 17 and 18, while correctly recovering the temporal characteristics of a source function, are uncalibrated in amplitude. To overcome this shortcoming, we normalize the recovered source functions, which are ramp-steplike, to their maximum value. The result is the source function denoted by $\hat{S}(t)$. Then, using the waveform synthesis program of Ceranoglu and Pao,[16] we can compute the normalized displacement signals, i.e., $\hat{u}_3^m(t)$ and $\hat{u}_3^d(t)$, corresponding to the normalized source functions $\hat{S}^m(t)$ of the monopolar source and $\hat{S}^d(t)$ of the dipolar source, respectively. Dividing Eq. (17) by Eq. (16) then yields for the dipole strength D an expression written in terms of the measured capacitive transducer voltage signals and the computed, normalized displacement signals

$$D = F_3H\left(\frac{V_0^d}{\hat{u}_3^d}\right)\Big/\left(\frac{V_0^m}{\hat{u}_3^m}\right). \tag{21}$$

Equation (21) is used for the determination of D, which will be described in Sec. IV.

D. Relation between the dipole source and fracture mechanics

The Dugdale–Barenblatt model[8–10] was chosen to make the connection between the AE source dipole strength and fracture mechanics. This model is well suited for the explanation of crack formation both in plastic solids (Dugdale

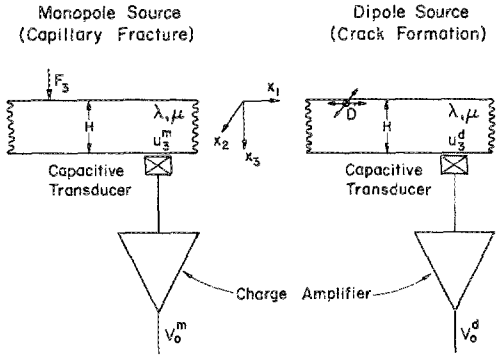

FIG. 8. Diagrams indicating the configuration of monopolar an dipolar sources and off-epicentral receivers. The capacitive transducer and charge amplifier shown in each configuration are the same.

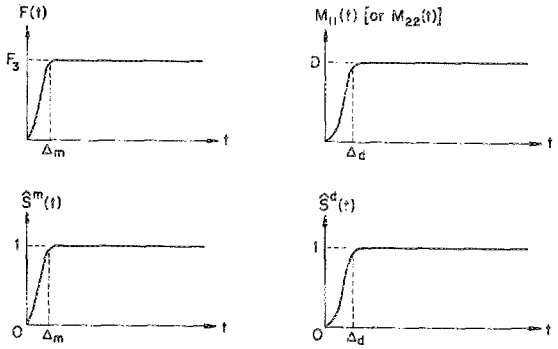

FIG. 9. Schematic of the monopolar and dipolar source-time functions.

model) and in brittle solids (Barenblatt model). The essential feature of the Dugdale–Barenblatt model is the laminar geometry of the separation process, consistent with the assumptions involved in the formulation of Rice's J integral.[19] Crack growth in this model is described as the sequential rupture of microstructural linkage units of length l with the critical rupture displacement u_c across the crack plane. In the Barenblatt theory, l is identified as the size of the cohesive zone surrounding the crack plane. A balance between the distributions of macroscopic opening stresses and microscopic closing stresses is maintained across the zone boundary between the outer, linear and the inner, cohesive zones. The opening stresses are those resulting from the load applied through the indenter and transmitted through the outer, linear material while the closing stresses are imposed by the cohesive bond forces acting across the crack plane.

The sequential rupture of microstructural units of length l, as the Vickers indentation crack advances from the indenter tip to the final crack dimension R, is translated into the dropout of the critical closing stress σ_c at the zone boundary between the inner cohesive zone of length l surrounding the crack tip and the outer linear zone, as the Dugdale–Barenblatt model postulates. The dropout of σ_c comprises a tensile dipole. Denoting the area swept by the crack front by $A(t)$ whose final size A_f is equal to $(1/2)\pi R^2$, the area of the half-penny crack, the dipole function $D\hat{S}^d(t)$ can be expressed as

$$D\hat{S}^d = \sigma_c A(t) l = (\tfrac{1}{2})\pi\sigma_c l r^2(t), \tag{22}$$

where $r(t)$ is a radius of the crack front at some instant of time between crack initiation and crack arrest. In the context of acoustic emission, l corresponds to the dipole linkage distance and $A_f l$ may be called the AE source volume. Remembering that when $t \gg \Delta_d$, $\hat{S}^d(t) = 1$, and $A(t) = A_f$, one obtains from Eqs. (3), (4), and (22) expressions for D, ϵ_c, σ_c, u_c, and l. The results are

$$D = \sigma_c A_f l = E A_f u_c, \tag{23}$$

$$\epsilon_c = 2G_c A_f / D, \quad \sigma_c = E\epsilon_c = 2EG_c A_f / D, \tag{24}$$

$$u_c = D/EA_f, \quad l = u_c/\epsilon_c = D^2/2EG_c A_f^2. \tag{25}$$

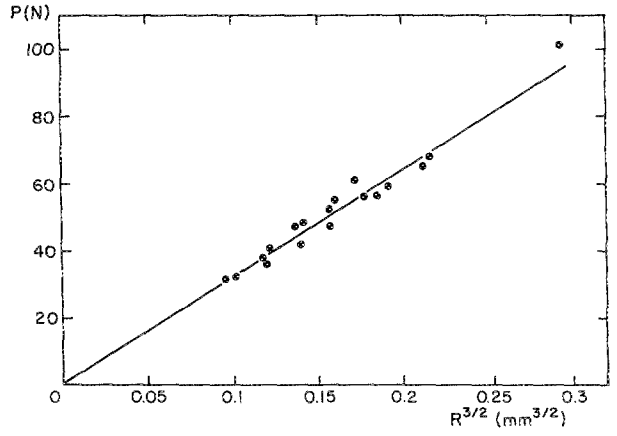

FIG. 10. A plot of applied load P vs $R^{3/2}$. R is an average crack radius. The straight line is a least-squares fit to the data.

A relationship between the applied load P and the calculated dipole strength D can be found from Eqs. (1), (2), and (23). It is

$$\frac{P^2}{R} = \frac{\pi^2 \tan^2\psi}{1-\nu^2}\sigma_c D = 63.45\sigma_c D. \tag{26}$$

This equation predicts that a plot of (P^2/R) vs D will be a straight line whose slope is $63.45\sigma_c$.

The linear crack velocity v_c, defined as (dr/dt), can be obtained by differentiating Eq. (22) with respect to time with the result

$$v_c = \frac{dr}{dt} = \frac{A_f}{\pi r}\frac{d\hat{S}^d(t)}{dt}. \tag{27}$$

Combining Eq. (27) with Eq. (22), one can obtain a crack velocity at any instant of time or at any radius of the crack front during its formation.

IV. RESULTS

The applied load P at a time of crack formation versus $R^{3/2}$ is shown in Fig. 10. The values of both P and R are listed in Table I. A least-squares fit yields a slope of (324.4 ± 5.0) N/mm$^{3/2}$ from which one obtains with Eqs. (1)–(3)

$$\begin{aligned} K_{Ic} &= (0.744 \pm 0.012) \quad (\text{MN/m}^{3/2}), \\ G_c &= (7.23 \pm 0.23) \quad (\text{J/m}^2), \\ \gamma &= (3.62 \pm 0.12) \quad (\text{J/m}^2), \end{aligned} \tag{28}$$

The fracture surface energy γ for soda-lime glass listed above compares well with the previous result of Wiederhorn[20] of 3.91 J/m^2, which was obtained by using a double-cantilever beam testing method. The values of γ cited in the literature[20–22] range from 3 to 10 J/m^2, depending on such factors as the test method employed, prepared crack tip shape, loading condition, environmental factors, and others.

The plate Green's functions shown in Fig. 7 are those for a plate having free boundaries. The AE signals detected at the epicenter are found to be affected by the effects of the Vickers diamond impression and thus include an extraneous P-wave contribution resulting from its reflection from the indenter/specimen boundary rather than from a free surface. This effect is much less pronounced in the off-epicentral signals, which were used to determine the source dipole strength and its time function. A typical example of a source-time function, $\hat{S}^d(t)$ associated with crack No. 7, was obtained by deconvoluting the off-epicentral signal detected at a 0° position (see Fig. 3) with the corresponding Green's function shown in Fig. 7(b). The resulting time function was normalized so that it has unit amplitude for times $t \gg \Delta_d$. The result is shown in Fig. 11(a). Synthesized waveforms, obtained by convoluting the resulting time function $D\hat{S}^d(t)$ with the same Green's function, are shown in Fig. 3 as dotted lines for receivers at $\theta = 0°$, 45°, and 90°. Similar procedures were used to obtain the source-time function $\hat{S}^m(t)$, and the recovered waveforms for the case of the capillary fractures. They are shown respectively in Fig. 11(b) and in Fig. 4 as dotted lines.

According to Eq. (21), a determination of the source dipole strength D requires the calculation of both $\hat{u}_3^q$ and $\hat{u}_3^m$.

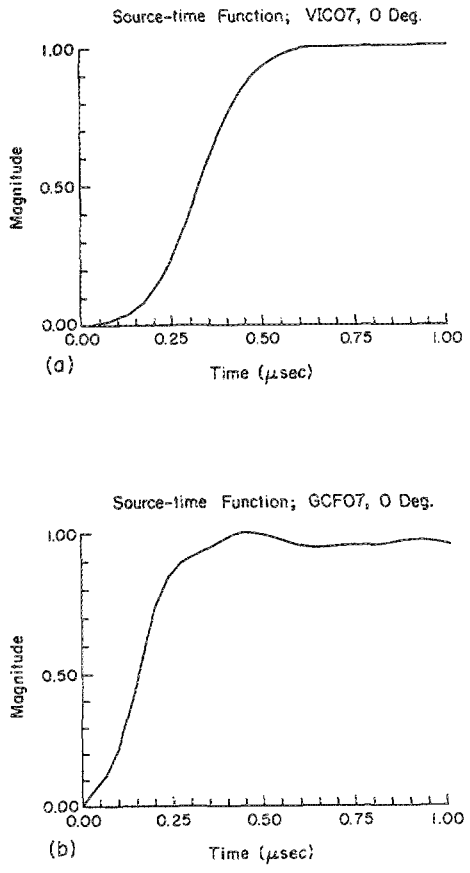

FIG. 11. Source-time functions of unit magnitude. (a) $\hat{S}^d(t)$. (b) $\hat{S}^m(t)$.

They are obtained by convoluting $\hat{S}^d(t)$ and $\hat{S}^m(t)$ as determined above with the corresponding Green's functions shown in Fig. 7, which were calculated using the algorithm developed by Ceranoglu and Pao.[16] Determination of both $(V_0^d/\hat{u}_3^d)$ and $(V_0^m/\hat{u}_3^m)$ in Eq. (21) requires special care. If V_0^d and $\hat{u}_3^d$ and likewise V_0^m and $\hat{u}_3^m$ are very similar, an ideal determination requires a synchronization of their wave arrivals, division of the entire waveforms point-by-point, and then choosing an averaging algorithm to smoothen the result. Unfortunately, the results often depend critically upon the smaller amplitudes and the zero crossings in the signals, as can be seen in Figs. 3 and 4. One way of avoiding these problems is to process only the amplitude of the first P-wave arrival. However, this amplitude is strongly affected by the source-time function $\hat{S}^d(t)$. The arrival of the P-wave signal is evidenced in the normal displacement signal as a sharp pulse as shown in Fig. 3, in which the amplitude is very sensitive to a small change in the source-time function. The approach taken by us to circumvent these difficulties and to minimize the errors was to use the signal amplitudes of extreme value found after the arrival of the S wave, which is the broad peak identified in Figs. 3 and 4. Values of both $(V_0^d/\hat{u}_3^d)$ and $(V_0^m/\hat{u}_3^m)$ for the determination of the dipole strength D are those determined at an extremum amplitude point found after the arrival of the S wave as shown in Figs. 3 and 4. These amplitudes are denoted as $(V_0^d/\hat{u}_3^d)s$ and $(V_0^m/\hat{u}_3^m)s$, respectively, in Table II. Listed also in this table are the strengths of the glass capillary fracture F_s and the calculated dipole strengths D for each of the detected off-epicentral AE signals.

The dipole strengths listed in Table II are generally of equal magnitude when determined from the signals associated with the same crack, detected at the three off-epicentral transducer positions, equidistant from the location of the source. According to Eq. (14), the AE signals from a Vickers generated crack are expected to exhibit a circular radiation pattern. It is seen that for several cracks there is considerable scatter in the recovered dipole strength. The exact reason for this is not clear. It is likely the result of a combination of the finite waveform sampling rate, finite bandwidth of the signal detection system, transducer aperture effects, and errors resulting from the signal deconvolution procedure.

In Fig. 12 is a plot of P^2/R versus the dipole strength D. The slope of the straight line from the least-squares fit was found to be (567.4 ± 11.5) GPa. From Eq. (26) one obtains a critical rupture stress σ_c:

$$\sigma_c = (8.94 \pm 0.18) \text{ (GPa)}. \tag{29}$$

The corresponding critical rupture strain ϵ_c, the critical crack tip opening displacement u_c, and the effective gauge length l can be found from Eqs. (3) and (4). The results are

$$\begin{aligned} \epsilon_c &= 0.122 \pm 0.003, \\ u_c &= (1.62 \pm 0.09) \text{ (nm)}, \\ l &= (13.2 \pm 0.71) \text{ (nm)}, \end{aligned} \tag{30}$$

V. DISCUSSION

Using indentation fracture mechanics we obtained for soda lime glass a mode I stress intensity factor K_{Ic}, a strain energy release rate G_c, and the fracture surface energy γ. We calculated the dipole strength D associated with crack formation from the theory of acoustic emission. Based on the Barenblatt–Dugdale model and also on the assumption that the effective gauge length l can be interpreted as the dipole linkage distance, a relationship was established between the dipole strength and fracture mechanics according to Eq. (22), from which all the other relevant fracture mechanics parameters such as the critical rupture stress σ_c and the CTOD u_c could be determined as shown in Eqs. (29) and (30). Another important relationship governing the crack velocity will be discussed later in this section. The values of both σ_c and ϵ_c thus found are fairly close to those predicted for a perfectly brittle solid, 7.30 GPa and 0.1, respectively.[11] We also observe that the CTOD, $u_c = 1.62$ nm as shown in Eq. (30), is about 6–10 times as large as the characteristic atomic dimension of glass, such as the silicon-oxygen distance 0.16 nm or the oxygen-oxygen distance of 0.26 nm. It is also noted that the effective gauge length (or the size of the cohesive zone) involved in fracture process, $l = 13.2$ nm, encompasses about 80 nearest interatomic spacings.

Marsh[23] demonstrated plastic flow around indentations in the hardness test and correlated this flow with a yield stress σ_Y in glass. The plastic flow around a hardness indentation results from the very high stresses that exist around the indenter during the hardness test. Similar high stresses must exist in the vicinity of the crack tip just before fracture,

TABLE II. Relevant data for dipole strength.

Crack No.	Glass cap. fracture strength (N)	AE sensor position (deg)	$(V_0^d/\hat{u}_3^m)_s$ ($\times 10^4$)	$(V_0^m/\hat{u}_3^m)_s$	Dipole strength ($\times 10^5$ N m)
VIC01	5.786	0	0.843	0.407	1.151
		45	2.841	1.458	1.083
		90	1.404	0.606	1.286
VIC02	3.658	0	1.020	0.235	1.527
		45	2.375	0.610	1.368
		90	1.162	0.304	1.341
VIC03	5.168	0	1.088	0.358	1.509
		45	2.518	0.912	1.371
		90	1.278	0.425	1.492
VIC04	5.962	0	0.700	0.390	1.026
		45	2.323	1.400	0.950
		90	0.837	0.474	1.011
VIC05	5.060	0	0.849	0.325	1.268
		45	1.133	0.442	1.245
		90	1.027	0.400	1.249
VIC06	4.070	0	0.646	0.243	1.042
		45	0.340	0.134	0.989
		90	0.779	0.314	0.970
VIC07	3.187	0	4.122	0.584	2.158
		45	9.285	1.320	2.152
		90	4.904	0.670	2.240
VIC08	4.001	0	1.262	0.280	1.733
		45	2.904	0.623	1.792
		90	1.453	0.312	1.788
VIC09	5.737	0	0.509	0.410	0.685
		45	1.058	1.015	0.574
		90	0.554	0.439	0.703
VIC10	4.609	0	1.355	0.323	1.857
		45	2.464	0.805	1.354
		90	1.349	0.370	1.615
VIC11	3.393	0	2.085	0.684	0.993
		45	4.277	1.684	0.828
		90	2.290	0.758	0.984
VIC12	4.844	0	4.941	0.862	2.666
		45	13.24	1.899	3.247
		90	6.350	1.057	2.794
VIC13	3.217	0	9.303	0.595	4.830
		45	22.21	1.652	4.153
		90	11.18	0.807	4.511
VIC14	4.589	0	3.171	0.783	1.784
		45	6.531	1.947	1.478
		90	2.953	0.837	1.554
VIC15	3.256	0	4.546	0.644	2.208
		45	10.13	1.656	1.914
		90	3.136	0.624	1.572
VIC16	4.521	0	1.517	0.778	0.846
		45	2.938	1.892	0.674
		90	1.278	0.880	0.631
VIC17	3.844	0	4.612	0.644	2.645
		45	9.898	1.370	2.666
		90	4.024	0.683	2.176
VIC18	2.854	0	3.717	0.568	1.794
		45	5.258	0.983	1.465
		90	3.025	0.545	1.520

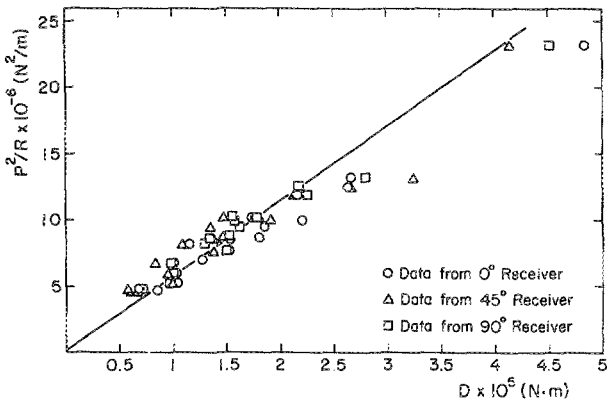

FIG. 12. A plot of P^2/R vs D (dipole strength). The straight line is a least-squares fit to the data.

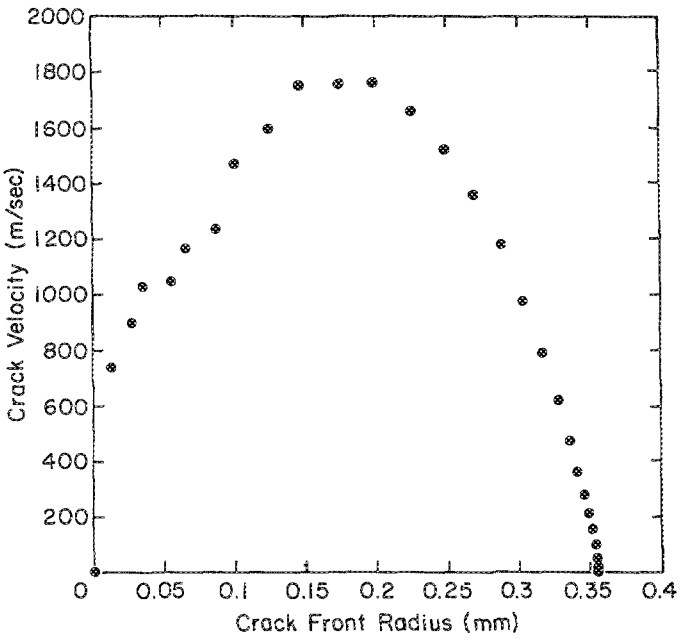

FIG. 13. Crack velocity of VIC07 as a function of the crack front radius.

and it is not unreasonable to suggest that plastic deformation might indeed initiate from the crack tip during fracture. From the indentation experiments, Marsh[23] found the yield stresses σ_Y of soda-lime glass and fused silica were 10.0 and 19.5 GPa, respectively, at liquid-nitrogen temperatures. Considering that the yield stress at room temperature is a little lower than that at liquid-nitrogen temperature, the critical rupture stress σ_c shown in Eq. (29) is close to the yield stress of the material. Using the simple relation $G_c = \sigma_Y u_c$ derived from the Dugdale model for fracture of plastic solids, u_c was found to be 0.072 nm, about half the nearest interatomic distance, and much smaller than the value 1.62 nm obtained from the theory of brittle fracture. Whether the Dugdale model is applicable to the description of indentation fracture of very brittle solids undergoing plastic deformation is questionable. For a thin plate of a ductile material subjected to plane stressses, the size of the plastic zone at the crack tip is almost equal to the CTOD (100% effective plastic strain) as, for example, in the yielding of a slotted steel plate. Hence, the effective microstructural gauge length l may be the size of the CTOD. In general, the CTOD is smaller than the effective plastic gauge length for a thick specimen subjected to plane strain. Taking into account that in ductile fracture only a small fraction of the fracture energy is released, the dipole linkage distance of acoustic emission should be much smaller than either the effective plastic gauge length or the CTOD.

Finally we turn our attention to the calculation of time-dependent crack velocity. As shown in Eq. (27), an accurate determination of the source-time function is essential for the correct calculation of the crack velocity. Unfortunately, the recovered source-time function $\hat{S}^d(t)$ is strongly affected by the aperture of the detecting transducer. This is an additional reason why the peak amplitude of the first P-wave arrival has not been used for the determination of the dipole strength as described in the previous section. The capacitive transducers used in this experiment had a diameter of 3 mm. An aperture of this magnitude alone can result in a rise-time increase of 0.23 μs. Noticing that $\hat{S}^d(t)$ seen in Fig. 11(a) has a rise time of about 0.5 μs, the crack velocity determined from $\hat{S}^d(t)$ in Fig. 11(a) may have an error as high as 50%. In principle, it is possible to correct for the aperture effect[24] and also to include a correction for any sensitivity differences associated with the sensing area of the capacitive transducer. However, this is a tedious procedure and it remains to be shown that a reliable source-time function can be recovered in this way. In order to reduce the transducer aperture-related error to a level less than 10%, when signals are detected that contain important information at frequencies up to 10 MHz, the sensor used should have an active element that is less than 0.5 mm in diameter. Such a sensor will, however, greatly reduce the overall sensitivity of the detection system and for this reason it was never used in the experiments described here. The most desirable way of obtaining $\hat{S}^d(t)$ is to use an epicentral signal for deconvolution with the Green's function. At the epicenter the aperture effect is minimized and even the 3-mm transducer is likely to result in less than a 10% error in crack velocity. Unfortunately, as explained in the previous section, the epicentral signal is corrupted with extraneous P-wave arrivals and was therefore not used for the recovery of $\hat{S}^d(t)$ or the dipole strength of cracks.

It is nonetheless interesting to see how the general profile of crack velocity behaves as a function of the crack front radius until the crack arrests. It is emphasized that the crack velocity determined by this procedure will be considerably less than its actual value. For example, the crack velocity of VIC07 is plotted in Fig. 13, which is obtained according to Eq. (27) from the source-time function $\hat{S}^d(t)$ shown in Fig. 11(a). It is seen that a maximum velocity of 1763 m/s is reached when the crack front radius is 0.175 mm, or about midway towards the final crack size. The time taken to reach the final crack size of 0.355 mm was 0.643 μs, from which one determines an average crack velocity of 522 m/s.

VI. CONCLUSIONS

Based on the results presented in this paper, the following conclusions can be drawn:

(1) The fracture surface energy and critical stress intensity factor were obtained from the measured data of applied load and crack size by using the formula derived from indentation fracture mechanics. These values compare well with those determined from other methods.

(2) The dipole strength and source time function associated with the formation of a crack can be determined from the theory of acoustic emission combined with signal processing techniques.

(3) Important fracture parameters of a crack, such as its critical rupture stress, crack tip opening displacement, and microstructural gauge length can be experimentally determined by combining AE theory with indentation fracture mechanics and the Dugdale–Barenblatt model.

(4) The crack velocity of a microindentation crack forming on a submicrosecond time scale can be obtained as a function of the crack position or time from the recovered source-time function of the crack and the measured final crack size.

ACKNOWLEDGMENTS

Early portions of this work were made possible by Grant No. MSM-8405466 from the National Science Foundation. Completion of this research was supported by the National Science Foundation through a grant of the Materials Science Center at Cornell University.

[1]B. R. Lawn and E. R. Fuller, J. Mater. Sci. **10**, 2016 (1975).
[2]B. R. Lawn and M. V. Swain, J. Mater. Sci. **10**, 113 (1975).
[3]A. G. Evans and T. R. Wilshaw, Acta Metall. **24**, 939 (1976).
[4]B. R. Lawn and R. Wilshaw, J. Mater. Sci. **10**, 1049 (1975).
[5]K. Y. Kim and W. Sachse, J. Appl. Phys. **59**, 2704 (1986).
[6]K. Y. Kim and W. Sachse, J. Appl. Phys. **59**, 2711 (1986).
[7]K. Y. Kim and W. Sachse, Rev. Sci. Instrum. **57**, 264 (1986).
[8]D. S. Dugdale, J. Mech. Phys. Solids **8**, 100 (1960).
[9]G. I. Barenblatt, Adv. Appl. Mech. **7**, 55 (1962).
[10]B. R. Lawn and T. R. Wilshaw, *Fracture of Brittle Solids* (Cambridge University Press, Cambridge, 1975), Chap. 4.
[11]E. Orowan, Rep. Prog. Phys. **12**, 48 (1949).
[12]K. Aki and P. G. Richards, *Quantitative Seismology: Theory and Methods* (Freeman, San Francisco, 1980), Vol. I, Chap. 3.
[13]D. J. Doornbos, in *Identification of Seismic Sources—Earthquake or Underground Explosion*, edited by E. S. Husebye and F. Mykkeltveit (Reidel, New York, 1981), pp. 207–232.
[14]K. Y. Kim and W. Sachse, Int. J. Fract. **31**, 211 (1986).
[15]P. M. Morse and H. Feshbach, *Methods of Theoretical Physics* (McGraw-Hill, New York, 1953), Part. I, Chap. 7.
[16]A. N. Ceranoglu and Y. H. Pao, J. Appl. Mech. **48**, 125 (1981); **48**, 133 (1981); **48**, 139 (1981).
[17]J. E. Michaels, T. E. Michaels, and W. Sachse, Mater. Eval. **39**, 1032 (1981).
[18]J. E. Michaels and Y. H. Pao, in *Review of Quantitative Nondestructive Evaluation*, edited by D. O. Thompson and D. E. Chimineti (Plenum, New York, 1984), Vol. 3, pp. 707–715.
[19]J. R. Rice, J. Appl. Mech. **35**, 379 (1968).
[20]S. M. Wiederhorn, J. Am. Ceram. Soc. **52**, 99 (1969).
[21]R. W. Davidge and G. Tappin, J. Mater. Sci. **3**, 165 (1968).
[22]J. Nakayama, J. Am. Ceram. Soc. **48**, 583 (1965).
[23]D. M. Marsh. Proc. R. Soc. London Ser. A **279**, 420 (1963).
[24]C. Chang and W. Sachse, in *Review of Quantitative Nondestructive Evaluation*, edited by D. O. Thompson and D. E. Chimenti (Plenum, New York, 1986), Vol. 5B, pp. 139–143.